



ARCHIVES  
of  
FOUNDRY ENGINEERING

ISSN (2299-2944)

Volume 2020

Issue 3/2020

92 – 98



10.24425/afe.2020.133336

16/3

Published quarterly as the organ of the Foundry Commission of the Polish Academy of Sciences

# Microstructure and Microhardness of Piston Alloy Al-10Si-2Cu Irradiated by Pulsed Electron Beam

D. Zaguliaev<sup>a</sup>, S. Konovalov<sup>b,\*</sup>, Y. Ivanov<sup>c</sup>, A. Abaturova<sup>a</sup>, A. Leonov<sup>c</sup>

<sup>a</sup>Siberian State Industrial University, Russia

<sup>b</sup>Samara National Research University, Russia

<sup>c</sup>Institute of High Current Electronics, Siberian Branch, Russian Academy of Sciences, Russia

\* Corresponding author. E-mail address: ksv@ssau.ru

Received 14.04.2020; accepted in revised form 03.06.2020

## Abstract

The paper presents the research data on structure, phase composition, defect substructure state, and microhardness of surface layers in the piston alloy Al-10wt%Si-2wt%Cu irradiated by an electron beam with various energy densities and pulse times. An important finding to emerge from the study is that the processing by an electron beam with an energy density of 10 J/cm<sup>2</sup> brings about slight surface melting, whereas a weak thermal impact of an electron beam hardly changes the phase composition. Once an energy density of an electron beam is set 30 J/cm<sup>2</sup>, intermetallic compounds dissolve and numerous micropores arise. Irradiating by an electron beam with an energy density of 50 J/cm<sup>2</sup>, randomly located microcracks are detected on the treated surface with no regard to a pulse time. A structure of high-speed cellular crystallization with cells from 500 to 600 nm forms in the surface layer. A thickness of the modified layer is related to a beam energy density. As a beam energy density goes up, a thickness of a high-speed cellular crystallization layer increases. Atoms of Si, Cu, Ni, as well as a small quantity of Fe and Mg are detected in the surface, in thin layers surrounding crystallization cells. In a layer 60-80 μm below the irradiated surface, in material between high-speed crystallization cells, there are Si atoms and an insignificant number of Cu atoms. An analysis of a deeper material part has shown a structure similar to the as cast alloy. A drop of microhardness – if compared with the as cast material – is reported at an energy density of 10 J/cm<sup>2</sup> because an energy amount supplied by an electron beam to the alloy surface is insufficient for melting of the material and dissolution of the intermetallic phase. A raise of a beam energy density up to 20-50 J/cm<sup>2</sup> causes a max increase of microhardness up to 1.13 GPa for 40 J/cm<sup>2</sup>, 50 μs, and up to 1.16 GPa for 40 J/cm<sup>2</sup>, 200 μs.

**Key words:** Al-10wt%Si-2wt%Cu alloy, Pulsed electron beam treatment, Microstructure, Phase composition, Microhardness

## 1. Introduction

The internal combustion engine has become an integral part of our life. Numerous agricultural tools (lawnmowers, fuel saws, cultivators, hole drills, etc.) are equipped with them. They are mounted in various transport means, from scooters to aircrafts.

A standard internal combustion engine suffers from certain drawbacks, first, it is the use of non-renewable resources (natural gas and petroleum products) and depletion of these resources, making their global prices go up, and second, it is the toxicity of exhaust emissions [1-6]. Under these circumstances researchers have to seek for a replacement to the traditional internal combustion engine or use alternative types of fuels [7-11]. Undoubtedly, the most popular up to date alternative is the

electric motor since it generates no harmful emissions into the atmosphere and its efficiency factor is much higher than that of the internal combustion engine [12-13]. However, the use of electric motors experiences a problem of power storage on a vehicle board. Rechargeable batteries mounted for this purpose are heavy, and their capacity decreases enormously as atmosphere temperature is below zero, so their use in northern latitudes is limited.

Another alternative is a hydrogen-driven motor, which is rightfully thought to be a future of the motor vehicle industry and may solve a problem of hazardous emissions and expensive fuel [14-17]. There are two categories of hydrogen-driven motors: units running on hydrogen-based fuel, and hydrogen-fueled internal combustion engines. The first ones generate electricity and are mountable in automobiles. The second group (hydrogen-fueled internal combustion engines) represents internal combustion engines running on hydrogen but having quite the same construction as petroleum-fueled internal combustion engines [18]. The capacity of the hydrogen-fueled motor is 20-40% lower than that of the gasoline-fueled engine [19-21]. This power loss may be eliminated via modifying the ignition system aimed at a temperature increase in a combustion chamber; as a result, the power might be up to 120 % higher in comparison to the gasoline version [22]. In most cases, it is reported on burnt out engine valves and pistons if a vehicle is operated at a high speed for a long time. Moreover, at temperatures and pressure generated in an engine, hydrogen can react with construction materials of an engine, causing its quick wear. Since aluminum alloys are used to manufacture most parts of internal combustion engines, the improvement of their strength, friction and corrosion properties is a burning issue of high practical relevance [23-26]. Properties of alloys depend on the structure and phase states of a material. A future modification process of structure and phase composition in aluminum and silicon alloys is suggested to be the processing by pulsed electron beams in a re-melting mode of surface layers [27-30].

The pulsed impact of an electron beam on the surface of metallic materials results in the melting and superfast crystallization in surface layers. A penetration depth relating to the energy of an electron beam may range to 100-200  $\mu\text{m}$  [31]. As a result of high-speed cooling, submicron and nano-dimensional structure and phase states develop in the surface layers, affecting immediately the strength, fatigue and tribology, etc. of the material [32-34].

In this context this work aims to reveal and analyze laws, which influence on the evolution of phase composition, defect substructure and microhardness of the surface in the piston alloy Al-10wt%Si-2wt%Cu irradiated by an electron beam with various energy densities and impact periods.

## 2. Material and methods

For the purpose of research, we used samples (10x10x5 mm<sup>3</sup>) of the piston alloy 10wt%Si-2wt%Cu, which were mechanically cut of a grinded and polished small as delivered ingot. The chemical composition of the alloy: 10.65 – Si; 2.11 – Cu; 0.89 – Ni; 0.85 – Mg; 0.26 – Fe; 0.03 – Mn; 0.05 – Ti; 0.01 – Pb; 0.02 – Zn; 0.01 – Cr; balanced Al, wt. %.

To irradiate samples by an intensive pulsed electron beam we used a laboratory unit “SOLO”. It consists of a pulsed electron source based on a plasma cathode with a grid stabilization of plasma boundary; a power supply unit of electron source; a vacuum technological chamber with an observation hole and a two-coordinate manipulator-table, where the plasma electron source and samples being irradiated are located; a control and monitoring system of electron source and electron beam parameters [35]. Electron beam parameters were set: energy of accelerated electrons – 17 keV, electron beam energy density – 10, 20, 30, 40 and 50 J/cm<sup>2</sup>, pulse duration – 50 and 200  $\mu\text{s}$ , number of impulses 3, time between impulses – 0.3 s<sup>-1</sup>; residual gas (argon) pressure in the processing chamber –  $2 \cdot 10^{-2}$  Pa; imprint diameter on a sample (electron beam signature) 2 – 5 cm.

The reported work was motivated by our previous research [36, 37]. Its key difference is other parameters describing the impact time of an electron beam.

The research into the phase and element composition, defect substructure state of the alloy was carried out using SEM (Philips SEM-515 equipped with a microanalyzer EDAX ECON IV) and TEM (JEM 2100F, which allows electron beam high sensitivity scanning (STEM-analysis), electron energy loss monitoring (EELS), and energy dispersive X-ray analysis of the foil element composition. SEM was conducted directly on the treated surface and on cross-sectional etched sections of irradiated samples. To prepare foils for the TEM research into the material structure-phase state, we used ion sputtering of plates cut by means of spark erosion perpendicular to the being irradiated surface. Cutting conditions were selected properly to avoid any unnecessary deformation and prevent from any effect on a sample structure.

## 3. Results and discussion

To begin with, we consider an alloy structure in the as cast state (Fig. 1) to identify irradiation-caused structural changes of a sample. It has been established that the alloy under study in the as delivered state is a polycrystalline aggregate containing grains of Al-based (1) solid solution and grains of Al-Si eutectics (2) (Fig. 1). In most cases, eutectics grains are located along boundaries and in Al-grain boundary junctions. An aluminum grain varies from 25  $\mu\text{m}$  to 100  $\mu\text{m}$ ; Al-Si eutectics grains are in a range from 10  $\mu\text{m}$  to 30  $\mu\text{m}$ . Additional phases in the material of interest are intermetallic compounds (designated by arrows Fig. 1b). Particles of intermetallic compounds in the alloy are supposed to affect the brittleness of the material when mechanically loaded, irrespectively to their morphology.

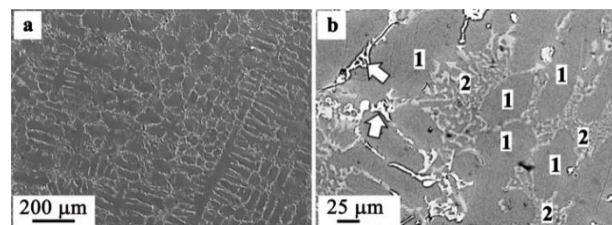


Fig. 1. Alloy structure in the as cast state; numbers (b) stand for: 1 – solid aluminum-based solution; 2 – eutectics grains; arrows indicate intermetallic compounds

Fig. 2 provides an electron-microscopic view of a treated surface, which was obtained in the course of SEM analysis for different electron beam energy densities and pulse times. Comparing the structure given in Fig. 2 with that in the as cast state (Fig. 1), its significant transformations caused by the pulsed electron-beam processing are apparent.

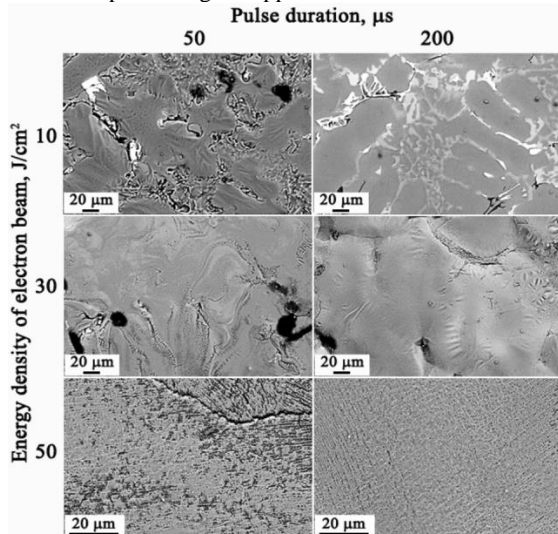


Fig. 2. The surface structure of the alloy Al-10wt%Si-2wt%Cu irradiated by a pulsed electron beam in a variety of modes

The treated surface looks wavy at a beam energy density of 10 J/cm<sup>2</sup>, being an evidence of its primary melting. Similarly to the as cast state, the structure contains three phases: grains of aluminum-based solid solution, eutectics, and intermetallic compounds. Intermetallic compounds tend to dissolve at a beam energy density of 30 J/cm<sup>2</sup>, and numerous pores arise, probably for the material shrinkage when crystallizing at a high speed. Lengthy layers made of round particles (0.5-0.6 μm) form instead of formerly located intermetallic compounds. The study has pointed out randomly located microcracks on the irradiated surface at a beam energy density of 50 J/cm<sup>2</sup> irrespectively to a pulse time. It is suggested they develop due to inner stresses generating in the material surface as the liquid layer cools down at high speeds and crystallizes on the integrally cold substrate. A high-speed cellular crystallization structure with cells in a range 500-650 nm forms in a developing surface layer.

Fig. 3 demonstrates typical electron-microscopic views of etched cross-sectional sections in the alloy Al-10wt%Si-2wt%Cu irradiated by a pulsed electron beam. From the data it is apparent a thickness of the modified layer depends on a beam energy density: 1-2 μm at 10 J/cm<sup>2</sup>; 25-30 μm at 30 J/cm<sup>2</sup>; and 60-90 μm at 50 J/cm<sup>2</sup>. The processing by an electron beam of 30 and 50 J/cm<sup>2</sup> results in the dissolution of silicon and intermetallic compounds found in the as delivered structure, irrespectively to a pulse time.

The most significant finding to emerge from a TEM-based analysis is that the irradiation by an electron beam with an energy density of 10 J/cm<sup>2</sup> and various pulse times leads to melting of aluminum only in the most examined zones of the alloy surface under study. Crystallites of silicon and intermetallic compounds

fail to dissolve completely because of a weak thermal impact produced by an electron beam.

Fig. 4 instances a forming structure given that silicon crystallites dissolve partly. The data show that a high-speed cellular crystallization structure of aluminum forms around silicon inclusions in the course of high-speed heating and cooling (Fig. 4a). Boundaries of cells are surrounded by particles of the second phase containing silicon atoms on a large scale (Fig. 4b). It will be observed a thickness of a thin layer surrounding silicon crystallites and modified by an electron beam decreases at a distance below the irradiated surface, furthermore, this layer is not detected at a distance of 10-12 μm. This fact may indicate indirectly a thickness of the layer where aluminum contacting with silicon crystallites tends to melt.

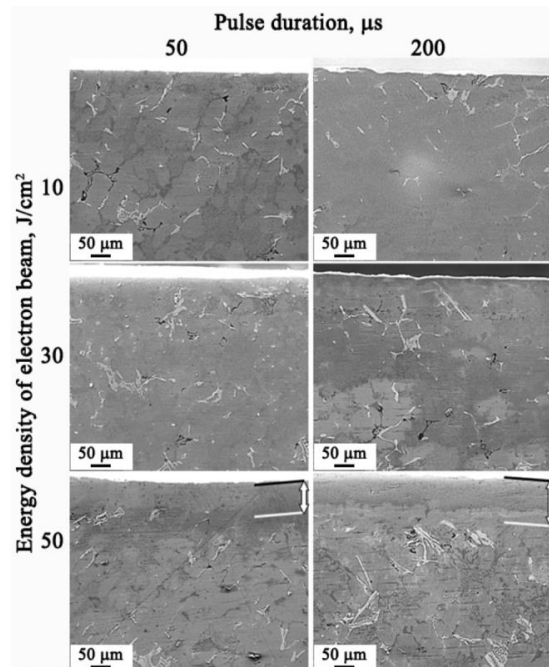


Fig. 3. The structure of a cross-sectional etched section in the alloy Al-10wt%Si-2wt%Cu irradiated by a pulsed electron beam in a variety of modes

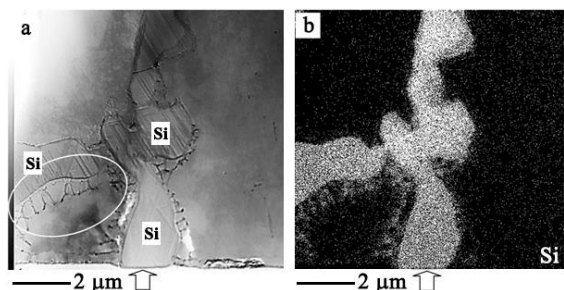


Fig. 4. The surface layer of the alloy of interest irradiated by a pulsed electron beam (10 J/cm<sup>2</sup>, 200 μs) imaged in STEM (a) and characteristic X-ray emission of silicon atoms (b). Arrows indicate the treated surface of a sample. A foil zone (a) is circled where electron-microscopic micro-diffraction analysis was carried out

Fig. 5 provides the research data on a circled zone (Fig. 4a) investigated in an energy dispersive X-ray analysis. As seen (Fig. 5a), high-speed crystallization cells of aluminum are oval, transversal sizes of cells range from 100 nm to 300 nm; samples are 150 to 450 nm lengthwise. The cells are surrounded by second phase thin layers with a thickness of 40-75 nm. The structure of layers is nano-dimensional; the crystallites vary from 5 to 10 nm (Fig. 5c). From the data of micro-electron diffraction pattern (Fig. 5b) obtained on this foil section it is apparent silicon particles constitute these layers (Fig. 5c). Nano-dimensional particles are detected in the volume of cells. Besides silicon particles, particles of other phases might form in the layers. Fig. 4d gives the data confirming the formation of  $\text{CuAl}_2$  phase in layers.

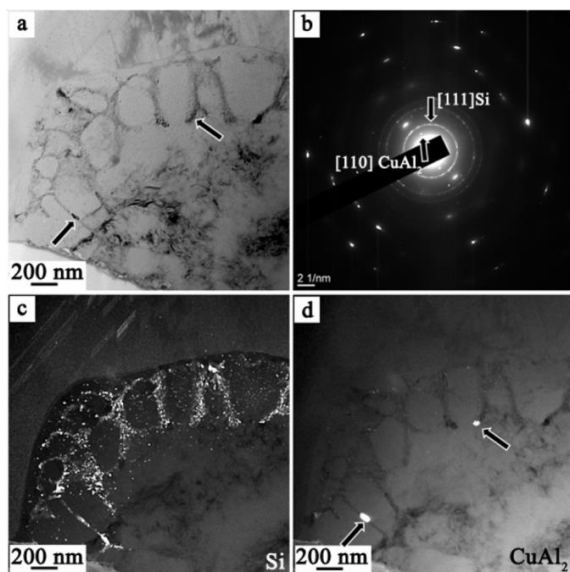


Fig. 5. Electron-microscopic view of a surface structure in the alloy under consideration irradiated by a pulsed electron beam  $10 \text{ J/cm}^2$ ,  $200 \mu\text{s}$ ; a – bright field; b – micro-electron diffraction pattern, obtained on a foil section (a); c, d – dark fields obtained in reflexes  $[111]\text{Si}$  and  $[110]\text{CuAl}_2$ , respectively

A thickness of a cellular crystallization layer goes up in conjunction with an increasing density of an electron beam (for any pulse time of a beam), being  $\approx 90 \mu\text{m}$  at  $50 \text{ J/cm}^2$ . An energy dispersive X-ray analysis has shown that the element composition of layers surrounding crystallization cells is directly related to a space between them and the irradiated surface. The study has detected atoms of silicon, copper, and nickel, as well as a small amount of iron and magnesium (Fig. 6 a-d) in a surface up to  $60 \mu\text{m}$ , in thin layers, separating crystallization cells. With regard to the element composition of thin layers this alloy layer is supposed to be a result of melting and high-speed crystallization of all phases constituting the material (aluminum, silicon, and intermetallic compounds).

In a layer  $60\text{-}80 \mu\text{m}$  below the processed surface, in thin layers, surrounding high-speed crystallization cells, there are silicon atoms and a small quantity of copper atoms (Fig. 6 e-h). Assumingly, this material layer is a product of melting and subsequent high-speed crystallization of aluminum grains and

silicon crystallites. Almost all inclusions of intermetallic compounds failed to dissolve in this layer.

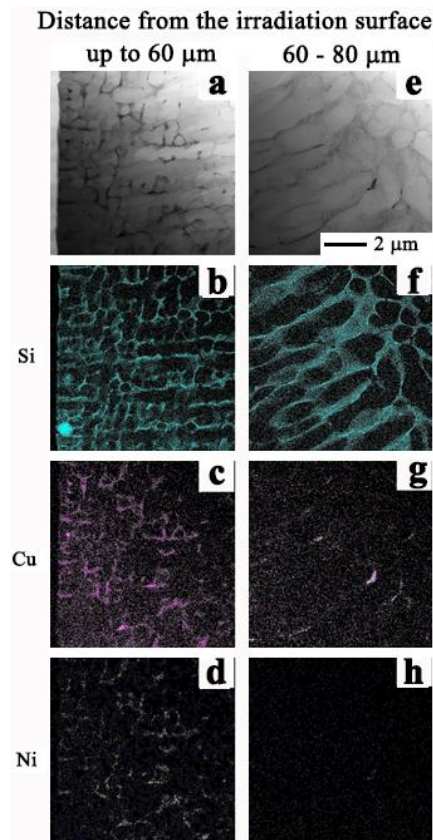


Fig. 6. Surface layers of the alloy  $\text{Al-10wt}\%\text{Si-2wt}\%\text{Cu}$  irradiated by a pulsed electron beam (a beam energy density  $50 \text{ J/cm}^2$ ) imaged in STEM (a, e) and in characteristic X-ray emission of silicon (b, f), copper (c, g), and nickel (d, h) atoms; a-d – surface layer at a depth of approximately  $60 \mu\text{m}$ ; e-h – layer at a depth of  $60\text{-}80 \mu\text{m}$

The study has revealed a structure similar to that presented in Fig. 4 at a distance of  $80\text{-}90 \mu\text{m}$  below the irradiated surface, i.e. silicon crystallites, intermetallic compounds, and a cellular crystallization structure around silicon crystallites. Probably, conditions to further the melting of aluminum and partial dissolution of silicon crystallites were realized in this layer. As a result of the further high-speed cooling, a structure of cellular crystallization formed in the material close to silicon crystallites. A structure, resembling the as cast state, was found in a volume of the material at deeper distances from the irradiated surfaces.

We suggested these significant structural transformations in the surface of the alloy  $\text{Al-10wt}\%\text{Si-2wt}\%\text{Cu}$  irradiated by a pulsed electron beam might affect properties of the surface. To characterize the surface properties, we measured microhardness in all conditions of modification directly on the irradiated surface. Results of measurements are given in Fig. 7. The microhardness of the as cast alloy is as much as  $0.72 \text{ GPa}$ . To simplify the analysis of microhardness this value is selected to be a cross point of X and Y axes in Fig. 7.

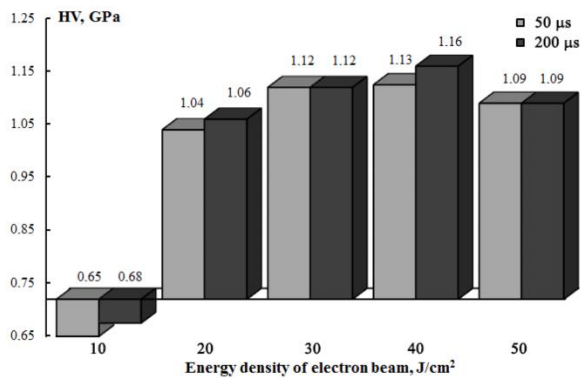


Fig. 7. Behavior of microhardness in surface layers of the alloy Al-10wt%Si-2wt%Cu irradiated by a pulsed electron beam with various energy densities and time between pulses. A cross point of X and Y axes refers to the microhardness in the as cast state

From the bar diagram it is seen that the microhardness decreases insignificantly if treated by a pulsed electron beam with an energy density of 10 J/cm<sup>2</sup>. This fact is probably related to an amount of energy supplied by an electron beam to the surface, which is insufficient for re-melting of the material and dissolution of the intermetallic phase. A raise of a beam energy density up to 20-50 J/cm<sup>2</sup> increases microhardness up to 1.1 GPa on average. It is important, that the microhardness hardly correlates with a pulse time of an electron beam. Obviously, these transformations are caused by a forming nano-crystalline cellular crystallization structure and the dissolving intermetallic phase.

## 4. Conclusion

The study focused on the effect of intensive pulsed electron beam in a variety of conditions, e.g. energy density and time between pulses on the structure and properties of the piston alloy Al-10wt%Si-2wt%Cu has concluded an electron beam with an energy density of 10 J/cm<sup>2</sup> having an insignificant thermal impact brings about the primary melting of a material surface, whereas no transformations are registered in the phase composition. Intermetallic compounds dissolve at a beam energy density of 30 J/cm<sup>2</sup>, as well as numerous micropores form as high-speed crystallization causes material shrinkage. Given that a beam energy density is 50 J/cm<sup>2</sup>, chaotically located microcracks initiate on the irradiated surface due to inner stresses arising in the material surface when a liquid layer to crystallize on an integrally cold base cools down at high-speeds. If irradiated in these conditions, a surface layer has a structure of cellular crystallization with cells in a range from 500 to 650 nm.

The research has pointed out a thickness of the modified layer to depend directly on a beam energy density, being 1-2 µm at 10 J/cm<sup>2</sup>, 25-30 µm at 30 J/cm<sup>2</sup>, and 60-90 µm at 50 J/cm<sup>2</sup>, and not connected with a pulse time (50 or 200 µs). The modified layer has a structure of high-speed cellular crystallization.

An energy dispersive X-ray analysis has detected silicon, copper, nickel, and an insignificant quantity of iron and magnesium in the surface (not deeper than 60 µm) in thin layers to separate crystallization cells. There are silicon atoms and a

small amount of copper in thin layers to surround high-speed crystallization cells at a depth of 60-80 µm. Silicon crystallites, intermetallic compounds, and a structure of cellular crystallization around silicon crystallites were detected in a layer 80-90 µm below the irradiated surface. An analysis of a deeper material part has shown a structure similar to the as cast alloy.

A relation between microhardness and beam energy density is non-monotonous for various pulse times, e.g. in comparison to the as cast state microhardness decreases at an energy density of 10 J/cm<sup>2</sup>, a further raise of a beam energy density up to 20-50 J/cm<sup>2</sup> increases microhardness, which is maximal (1.16 GPa) for a beam energy density of 40 J/cm<sup>2</sup> and pulse time 200 µs. The study has revealed no dependence of microhardness upon pulse time of an electron beam.

## Acknowledgements

The research was funded by Russian Science Foundation (RSF) under the project № 19-79-10059.

## Reference

- [1] Hongfang, L., Lijun, G., Mohammadamin, A. & Kun, H. (2019). Oil and Gas 4.0 era: A systematic review and outlook. *Computers in Industry*. 111, 68-90. DOI: 10.1016/j.compind.2019.06.007.
- [2] Szwaja, S., Ansari, E., Rao, S., Szwaja, M., Grab-Rogalinski, K., Naber, J.D. & Pyrc, M. (2018). Influence of exhaust residuals on combustion phases, exhaust toxic emission and fuel consumption from a natural gas fueled spark-ignition engine. *Energy Conversion and Management*. 165, 440-446. DOI: 10.1016/j.enconman.2018.03.075.
- [3] Agarwal, A.K., Ateeq, B., Gupta, T., Singh, A.P., Pandey, S.K., Sharma, N., Agarwal, R.A., Gupta, N.K., Sharma, H., Jain, A. & Shukla, P.C. (2018). Toxicity and mutagenicity of exhaust from compressed natural gas: Could this be a clean solution for megacities with mixed-traffic conditions?. *Environmental Pollution*. 239, 499-511. DOI: 10.1016/j.envpol.2018.04.028.
- [4] Norhafana, M., Noor, M.M., Hairuddin, A.A., Hari Krishnan, S., Kadirgama, K. & Ramasamy, D. (2020). The effects of nano-additives on exhaust emissions and toxicity on mankind. *Materials Today: Proceedings*. 22(3), 1181-1185. DOI: 10.1016/j.matpr.2019.12.110.
- [5] Omrani, M., Goriaux, M., Liu, Y., Martinet, S., Jean-Soro, L. & Ruban, V. (2020). Platinum group elements study in automobile catalysts and exhaust gas samples. *Environmental Pollution*. 257, 113477. DOI: 10.1016/j.envpol.2019.113477.
- [6] Gremminger, A., Pihl, J., Casapu, M., Grunwaldt, J., Toops, T.J. & Deutschmann, O. (2020). PGM based catalysts for exhaust-gas after-treatment under typical diesel, gasoline and gas engine conditions with focus on methane and formaldehyde oxidation. *Applied Catalysis B: Environmental*. 265, 118571. DOI: 10.1016/j.apcatb.2019.118571.

- [7] Long, R., Zhao, Y., Luo, Z. & Liu, W. (2020). Alternative thermal regenerative osmotic heat engines for low-grade heat harvesting. *Energy*. 195, 117042. DOI: 10.1016/j.energy.2020.117042.
- [8] Erdiwansyah, Mamat, R., Sani, M.S.M., Sudhakar, K., Kadarohman, A. & Sardjono, R.E. (2019). An overview of Higher alcohol and biodiesel as alternative fuels in engines. *Energy Reports*. 5, 467-479. DOI: 10.1016/j.egy.2019.04.009.
- [9] Fayad, M.A., Tsolakis, A. & Martos, F.J. (2020). Influence of alternative fuels on combustion and characteristics of particulate matter morphology in a compression ignition diesel engine. *Renewable Energy*. 148, 962-969. DOI: 10.1016/j.renene.2019.10.079.
- [10] Sadeq, A.M., Bassiony, M.A., Elbashir, A.M., Ahmed, S.F. & Khraisheh, M. (2019). Combustion and emissions of a diesel engine utilizing novel intake manifold designs and running on alternative fuels. *Fuel*. 255, 115769. DOI: 10.1016/j.fuel.2019.115769.
- [11] Mohd Noor, C.W., Noor, M.M. & Mamat, R. (2018). Biodiesel as alternative fuel for marine diesel engine applications: A review. *Renewable and Sustainable Energy Reviews*. 94, 127-142. DOI: 10.1016/j.rser.2018.05.031.
- [12] Song, C.H. & Aaldering, L.J. (2019). Strategic intentions to the diffusion of electric mobility paradigm: The case of internal combustion engine vehicle. *Journal of Cleaner Production*. 230, 898-909. DOI: 10.1016/j.jclepro.2019.05.126.
- [13] Chung, C.T., Wu, C.-H. & Hung, Y.-H. (2020). Evaluation of driving performance and energy efficiency for a novel full hybrid system with dual-motor electric drive and integrated input- and output-split e-CVT. *Energy*. 191, 116508. DOI: 10.1016/j.energy.2019.116508.
- [14] Verhelst, S. & Wallner, T. (2009). Hydrogen-fueled internal combustion engines. *Progress in Energy and Combustion Science*. 35(6), 490-527. DOI: 10.1016/j.peccs.2009.08.001.
- [15] Takagi, Y., Oikawa, M., Sato, R., Kojiya, Y. & Mihara, Y. (2019). Near-zero emissions with high thermal efficiency realized by optimizing jet plume location relative to combustion chamber wall, jet geometry and injection timing in a direct-injection hydrogen engine. *International Journal of Hydrogen Energy*. 44(18), 9456-9465. DOI: 10.1016/j.ijhydene.2019.02.058.
- [16] Luo, Q., Hu, J.-B., Sun, B., Liu, F., Wang, X., Li, C. & Bao, L. (2019). Effect of equivalence ratios on the power, combustion stability and NO<sub>x</sub> controlling strategy for the turbocharged hydrogen engine at low engine speeds. *International Journal of Hydrogen Energy*. 44(31), 17095-17102. DOI: 10.1016/j.ijhydene.2019.03.245.
- [17] Zareei, J. & Rohani, A. (2020). Optimization and study of performance parameters in an engine fueled with hydrogen. *International Journal of Hydrogen Energy*. 45(1), 322-326. DOI: 10.1016/j.ijhydene.2019.10.250.
- [18] Zhu, H. & Duan, J. (2019). Research on emission characteristics of hydrogen fuel internal combustion engine based on more detailed mechanism. *International Journal of Hydrogen Energy*. 44(11), 5592-5598. DOI: 10.1016/j.ijhydene.2018.08.044.
- [19] Zhu, H., Zhang, Y., Liu, F. & Wei, W. (2020). Effect of excess hydrogen on hydrogen fueled internal combustion engine under full load. *International Journal of Hydrogen Energy*. DOI: 10.1016/j.ijhydene.2019.12.022.
- [20] Xu, P., Ji, C., Wang, S., Bai, X., Cong, X., Su, T. & Shi, L. (2019). Realizing low emissions on a hydrogen-fueled spark ignition engine at the cold start period under rich combustion through ignition timing control. *International Journal of Hydrogen Energy*. 44(16), 8650-8658. DOI: 10.1016/j.ijhydene.2019.01.275.
- [21] Yuan, C., Jing, Y., Liu, C. & He, Y. (2019) Effect of variable stroke on fuel combustion and heat release of a free piston linear hydrogen engine. *International Journal of Hydrogen Energy*. 44(36), 20416-20425. DOI: 10.1016/j.ijhydene.2019.05.232.
- [22] Millikin, M. (2006, February). *Hydrogen Internal Combustion Engines as a Transitional Technology, Hydrogen Internal Combustion Engine Symposium*. Retrieved February, 2006, from [https://www.greencarcongress.com/2006/02/hydrogen\\_intern.html](https://www.greencarcongress.com/2006/02/hydrogen_intern.html)
- [23] Esmeralda, A.G., Arenas-García, H., Rodríguez, A.F., Talamantes-Silva, J., Torres, R., Garza-Montes-de-Oca, N.F. & Colás, R. (2019). Thermal diffusivity of Al-Si cast alloys for internal combustion engines. *Thermochimica Acta*. 675, 172-179. DOI: 10.1016/j.tca.2019.03.020.
- [24] Rea, J.E., Oshman, C.J., Singh, A., Alleman, J., Buchholz, G., Parilla, P.A., Adamczyk, J.M., Fujishin, H.-N., Ortiz, B.R., Braden, T., Bensen, E., Bell, R.T., Siegel, N.P., Ginley, D.S. & Toberer, E.S. (2019). Prototype latent heat storage system with aluminum-silicon as a phase change material and a Stirling engine for electricity generation. *Energy Conversion and Management*. 199, 111992. DOI: 10.1016/j.enconman.2019.111992.
- [25] Liu, K., Chen, X., Shen, Q., Pan, Z., Singh, R.A., Jayalakshmi, S. & Konovalov, S. (2020). Microstructural evolution and mechanical properties of deep cryogenic treated Cu-Al-Si alloy fabricated by Cold Metal Transfer (CMT) process. *Materials Characterization*. 159, 110011. DOI: 10.1016/j.matchar.2019.110011.
- [26] Kolonakov, A.A., Kukhareenko, A.V., Deev, V.B. & Abaturova, A.A. (2015). Structure and chemical composition of the AK12MMgN piston alloy fabricated based on various charges. *Russian Journal of Non-Ferrous Metals*. 56(4), 428-433. DOI: 10.3103/S1067821215040094
- [27] Yan, P., Zou, J., Zhang, C. & Grosdidier, T. (2020). Surface modifications of a cold rolled 2024 Al alloy by high current pulsed electron beams. *Applied Surface Science*. 504, 144382. DOI: 10.1016/j.apsusc.2019.144382.
- [28] Bian, H., Aoyagi, K., Zhao, Y., Maeda, C., Mouri, T. & Chiba, A. (2020). Microstructure refinement for superior ductility of Al-Si alloy by electron beam melting. *Additive Manufacturing*. 32, 100982. DOI: 10.1016/j.addma.2019.100982.
- [29] Jung, A., Buchwalder, A., Hegelmann, E., Hengst, P. & Zenker, R. (2018). Surface engineering of spray-formed aluminium-silicon alloys by plasma nitriding and subsequent electron beam remelting. *Surface and Coatings Technology*. 335, 166-172. DOI: 10.1016/j.surfcoat.2017.12.016.

- [30] Nahmany, M., Hadad, Y., Aghion, E., Stern, A. & Frage, N. (2019). Microstructural assessment and mechanical properties of electron beam welding of AlSi10Mg specimens fabricated by selective laser melting. *Journal of Materials Processing Technology*. 270, 228-240. DOI: 10.1016/j.jmatprotec.2019.02.025.
- [31] Deqiang, W., Xiaobing, W., Rong, W., Hongyang, C. (2018). Surface modification of 5CrMnMo steel with continuous scanning electron beam process. *Vacuum*. 149, 118-123. DOI: 10.1016/j.vacuum.2017.12.032.
- [32] Xuewei, T., Zhengjun, Y., Shasha, Z., Jun, L., Jing, L. (2018) Investigation on microstructure, mechanical and tribological properties of in-situ (TiB+TiC)/Ti composite during the electron beam surface melting. *Surface and Coatings Technology*. 337, 418-425 DOI: 10.1016/j.surfcoat.2018.01.054.
- [33] Panin, S.V., Vlasov, I.V., Sergeev, V.P., Maruschak, P.O., Sunder, R., Ovechkin, B.B. (2015) Fatigue life improvement of 12Cr1MoV steel by irradiation with Zr<sup>+</sup> ion beam. *International Journal of Fatigue*. 76, 3-10. DOI 10.1016/j.ijfatigue.2014.10.011.
- [34] Panin, S.V., Maruschak, P.O., Vlasov, I.V., Sergeev, V.P., Ovechkin, B.B., Neifeld, V.V. (2016) Impact toughness of 12Cr1MoV steel. Part 2 - Influence of high intensity ion beam irradiation on energy and deformation parameters and mechanisms of fracture. *Theoretical and Applied Fracture Mechanics*. 83, 82-92. DOI: 10.1016/j.tafmec.2015.12.009.
- [35] Konovalov, S., Gromov, V., Zaguliyaev, D., Ivanov, Y., Semin, A. & Rubannikova, J. (2019). Dispersion of Al-Si Alloy Structure by Intensive Pulsed Electron Beam. *Archives of Foundry Engineering*. 19(2), 79-84. DOI: 10.24425/afe.2019.127120.
- [36] Ivanov, Yu.F., Zaguliaev, D.V., Nevskii, S.A., Gromov, V.E., Sarychev, V.D. & Semin, A.P. (2019). Microstructure and properties of hypoeutectic silumin treated by high-current pulsed electron beams. *Progress in Physics of Metals*. 20(3), 447-484. DOI: 10.15407/ufm.20.03.447.
- [37] Gromov, V., Konovalov, S., Ivanov, Y., Zaguliaev, D., Petrikova, E. & Serenkov, Y. (2019). Evolution of structure-phase states of hypoeutectic silumin irradiated by intensive pulse electron beams. *Materials Research Express*. 6(7), 076574. DOI: 10.1088/2053-1591/ab1683.